Impact of Side Chain Extension on the Morphology and Electrochemistry of Phosphonated Poly(Ethylenedioxythiophene) Derivatives

Jonathan Hopkins, Daniel Ta, Antonio Lauto, Carly Baker, John Daniels, Pawel Wagner, Klaudia K. Wagner, Nigel Kirby, Claudio Cazorla, David L. Officer, and Damia Mawad*

One factor with great bearing on the electrochemical performance of conjugated polymers is the film morphology. A balance between crystalline and amorphous domains needs to be achieved for the polymer to have an optimal ionic-electronic conductance. Here, the morphological and electrochemical properties of poly(ethylenedioxythiophene) polymers functionalized with phosphonate groups separated by methylene and butylene alkyl spacers from the backbone are compared. Extending the spacer from methylene to butylene increases structural ordering in the solid state as revealed by grazing-incidence wide-angle X-ray scattering. However, the ordered domains are only short range, suggestive of a paracrystalline morphology in which ordered regions are separated by amorphous regions. This has a negative impact on the intermolecular charge transport. The longer spacer appears to have impeded the uptake of hydrated counterions, seen by the increase in the ionization potential and energy requirement for electrochemical switching, as well as the decrease in the volumetric capacitance. These results elucidate the advantages of having the phosphonate pendant group close to the backbone, separated only by a methylene spacer. This synthetic design likely facilitates hydrated counterions to accumulate around the polar phosphonate groups, close to the doped backbone where they can easily compensate the charge carriers formed upon oxidation.

1. Introduction

The organic nature of conjugated polymers affords them remarkable synthetic flexibility, as organic synthesis techniques can be used to tailor their design and achieve specific combinations of properties for a variety of applications such as organic solar cells,[1–3] electrochromic displays,[4,5] and bioelectronic devices.[6–8] One factor with great bearing on the electrochemical performance of conjugated polymers is the film morphology, including the arrangement and packing of individual polymer chains in the semicrystalline material. In crystalline domains with closely-packed, π-stacked chains, charge carriers can travel efficiently between polymer chains, resulting in a high charge carrier mobility.[9] These crystalline domains should also be sufficiently interconnected to allow the charge carriers to travel efficiently with high mobility through the entire film.[10] Meanwhile, amorphous regions contain disordered

J. Hopkins, J. Daniels, D. Mawad
School of Materials Science and Engineering
UNSW Sydney
Sydney, New South Wales 2052, Australia
E-mail: damia.mawad@unsw.edu.au
D. Ta, A. Lauto
School of Science
Western Sydney University
Locked Bag 1797, Penrith, New South Wales 2751, Australia

C. Baker, P. Wagner, K. K. Wagner, D. L. Officer
Intelligent Polymer Research Institute and ARC Centre of Excellence
for Electromaterials Science
University of Wollongong
Wollongong, New South Wales 2522, Australia
N. Kirby
Australian Synchrotron
800 Blackburn Road, Clayton, Victoria 3168, Australia
C. Cazorla
Departament de Física
Universitat Politècnica de Catalunya
Campus Nord B4-B5, Barcelona 08034, Spain
D. Mawad
Australian Centre for NanoMedicine
UNSW Sydney
Sydney, New South Wales 2052, Australia

polymer chains with fewer points of connection for intermolecular charge transport to occur. However, this disorder also provides free volume for counterions to more easily penetrate the film, compensating charge carriers generated during electrochemical switching, and enhancing the volumetric capacitance of the material.[11] We aimed in this work to elucidate this interplay between morphology and electrochemistry, focusing on the impact of the length of the alkyl spacer on the electrochemical activity in aqueous media of poly(ethylenedioxythiophene) (PEDOT) functionalized with phosphonate groups.
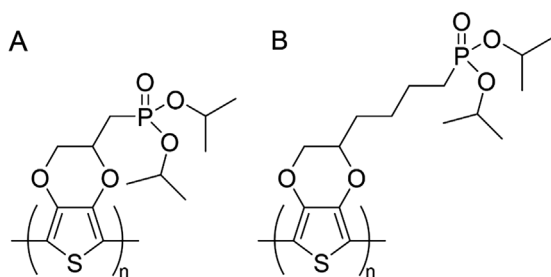
Given the substantial influence of morphology on the electrochemical properties of conjugated polymers, studies have focused on synthetic design of conjugated polymer derivatives with side chains of different molecular structures such as alkyl, alkoxy, glycolated, branched, bulky, and charged side chains.[7,12] This approach builds on early studies that have established the importance of the chemical structure, in particular the role of the side chains, on the morphology of dry films of functionalized conjugated polymers. For example, modulating the length of alkyl side chains has been extensively investigated in poly(3-alkylthiophene) (P3AT) derivatives. It was found that increasing the length of the alkyl side chain beyond six carbon atoms introduced steric hindrance, expanding the π-stacking distance between polymer chains in crystalline domains.[12–15] This corresponds to a greater hopping distance for intermolecular transport and results in a decrease in charge carrier mobility.[14,15] Other studies have investigated the effect of side chain length when the side chain is terminated by a bulky pendant group. Zhao et al.[16,17] synthesized homo- and copolymers of polythiophene derivatives bearing thermochromic azobenzene side groups, separated from the backbone by alkyl spacers with lengths ranging from four to eleven carbon atoms. The bulky side groups disrupted the ordered crystalline arrangement and decreased the number of crystalline reflections observed in X-ray diffraction. Increasing the length of the alkyl spacer still increased the π-stacking distance, but this increase was smaller when the bulky side groups were attached compared to P3ATs with no end groups. Wagner et al.[18] synthesized P3ATs with five carbon spacer atoms and additional carboxylic acid and ester terminal groups, and observed that dry films of both homopolymers and blends of these polymers exhibited poor structural ordering with no discernible π-stacking. On the other hand, a PEDOT derivative modified with an alkoxy chain terminated by a sulfonate and methyl group exhibited a semi-crystalline morphology with very high electrical conductivity.[19]

Besides the structure-property relationship, the impact of engineering the side chain on the structure-function relationship in conjugated polymers has also been investigated. It has been reported that a P3AT modified with an alkyl side chain having six carbon atoms performs best in organic photovoltaics.[14,20,21] The P3AT polymer bearing the 6-carbon alkyl side chain resulted in the highest charge carrier mobility and crystallinity compared to other side chain lengths. Shorter side chains caused phase segregation from acceptor components such as fullerene derivatives, resulting in lower mobility.[14,20] On the other hand, a solar cell based on a P3AT polymer modified with 5-carbon alkyl side chain and a non-fullerene acceptor was found to have the highest power conversion efficiency. This study also elucidated the role of odd- and even-numbered alkyl chains on the structure-

property relationship in solar cells. π–π stacking was enhanced in P3ATs with odd-numbered alkyl chains, in comparison to polymers having even-numbered side chains.[21] This odd-even effect was attributed to the van der Waals interactions of the carbon side chains and was shown to have an immediate effect on molecular packing. PEDOT derivatives functionalized with alkyl chains having six, ten, and fourteen carbon atoms have also been synthesized to tailor the performance of perovskite solar cells.[22] The PEDOT derivatives with a ten-carbon atom alkyl chain resulted in the best-performing photovoltaic cell, attributed to the formation of a uniform film and efficient hole transport.

Similarly, the impact of engineering the side chain on the morphology of conjugated polymers operating in an electrolyte has been investigated.[7,23] Here, the hydrophilicity/hydrophobicity of the side chain is a critical factor that influences the morphology of the functionalized polymer and its electrochemical performance. Hydrophilic side chains such as ethylene glycol facilitate ion injection and ion stabilization in the film, resulting in faster doping kinetics.[24–26] However, these side chains also disrupt any ordered domains which in turn impede charge transport. For example, Flagg et al.[27] reported that a high-crystallinity polythiophene derivative with a glycolated side chain exhibited low mobility, especially as the polymer swelled during electrochemical switching which interrupted the interconnectivity between crystalline domains. Hydrophobic side chains such as alkyl and alkoxy groups are used instead to limit excessive ion diffusion or tune the ionization potential (IP) of the polymer, respectively.[7,28] This in turn provides structural stability upon electrochemical switching. Nevertheless, hydrophobic side chains can have a detrimental effect on the volumetric capacitance of the polymer. An alternative synthetic design is to use hybrid side chains that combine both hydrophobic and hydrophilic groups, balancing effective ion diffusion with structural stability.[7,29] An example is the study by Ayalew et al.[30] reporting PEDOT derivatives with alkanoic acid pendant groups ranging from four to sixteen carbon atoms in length. They demonstrated that a nine-carbon spacer resulted in optimal back-bending of the side chain to compensate charge carriers in the backbone. In contrast, side chains with twelve carbons or more caused steric twisting of the backbone, resulting in lower conjugation lengths and higher oxidation onset potentials.

While it is established that side chain engineering has an impact on the morphology and thereby the structure-function property of conjugated polymers, the aforementioned studies demonstrate that when it comes to designing the side chain length, "one size does not fit all," and the effect of the pendant group on a polymer's morphological and electrochemical properties needs to be investigated on a case-by-case basis. Recently, we reported the first known derivative of PEDOT functionalized with pendant phosphonate groups (PEDOT-Phos).[31] The phosphonate pendant group was attached very close to the conjugated backbone, separated only by a methylene spacer (**Scheme** 1A). PEDOT-Phos exhibited efficient electrochemical switching in aqueous media with a low oxidation onset potential (−0.157 V vs Ag/AgCl), and a very high volumetric capacitance ($C^* = 282 \pm 62$ F cm^{-3}), representing one of the highest volumetric capacitances ever reported for a PEDOT-based conjugated polymer. These impressive electrochemical properties may be attributed to the very close proximity of the polar phosphonate pendant group to the conjugated backbone. As hydrated ions entered the film during

ADVANCED
SCIENCE NEWS

www.advancedsciencenews.com

ADVANCED
MATERIALS
TECHNOLOGIES

www.advmattechnol.de

Scheme 1. Chemical structures of A) PEDOT-Phos and B) PEDOT-Bu-Phos.

electrochemical switching, they likely accumulated around the polar phosphonate groups,[32,33] close to the doped backbone where they can easily compensate for the charge carriers formed upon oxidation. These hydrated ions around the phosphonate groups also pushed the nearby conjugated chains apart, generating a nanoporous morphology with a high internal surface area, yielding a very high volumetric capacitance.

Given the substantial effect of side chain length on morphological and electronic properties, we wanted to examine the effect of extending the side chain of phosphonated PEDOT. This would also elucidate the advantages of our previous synthetic design with the phosphonate pendant group very close to the backbone. Therefore, in this work, we compare the morphological and electrochemical properties of phosphonated PEDOTs with methylene and butylene alkyl spacers separating the dialkyl-protected phosphonate group from the conjugated PEDOT backbone (Scheme 1B). We chose to extend by only three carbons to limit any increase in the π-stacking distance, compared to six-carbon chains which are normally required to affect the π-stacking distance of alkyl-substituted PEDOTs.[22] We found that extending the spacer from methylene to butylene increased the degree of structural ordering in the solid state, but the ordered regions in the film were only short-range and did not enhance intermolecular charge transport. Extending the longer hydrophobic spacer also inhibited the uptake of hydrated counterions, seen by an increase in the IP and energy requirement for electrochemical switching. Similarly, the butylene spacer negatively impacted the volumetric capacitance, further evidence that the more hydrophobic spacer might have hindered ion diffusion in the film. These results provide valuable insight into optimizing the side chain functionalization of PEDOT derivatives in revealing that a very short, methylene spacer can afford optimal electrochemical properties in phosphonated PEDOTs, in contrast to other PT and PEDOT derivatives requiring much longer side chains.

2. Results and Discussion

2.1. Synthesis and Structural Characterization

We synthesized PEDOT-Bu-Phos in six steps as shown in Scheme S1, Supporting Information. Beginning with 3,4-dimethoxythiophene, we performed transetherification with 1,2,6-hexanetriol to achieve the molecule EDOT-Bu-OH bearing an extended side chain and a terminal hydroxyl functionality. This terminal hydroxyl was further functionalized via tosylate, iodide, and finally phosphonate moieties, using a pro-

tocol analogous to that used to synthesize our original EDOT-Phos.[31] We confirmed the successful synthesis of each of the four EDOT derivatives using one- and 2D solution NMR spectroscopy (Figures S1–S19, Supporting Information). Finally, oxidative polymerization of the phosphonated monomer followed by reduction with hydrazine monohydrate yielded the polymer PEDOT-Bu-Phos, which was soluble in chloroform allowing its processing into films for further characterization. We also synthesized PEDOT-Phos using our previously reported method.[31] Gel permeation chromatography (GPC) of PEDOT-Bu-Phos was performed in dimethyl formamide (DMF). The GPC measurements revealed a number-average molecular weight of $\bar{M}_n = 7859$ Da, corresponding to a polymer with 22 repeat units on average, and a weight-average molecular weight of $\bar{M}_w = 10\,903$ Da resulting in a dispersity $\bar{M}_w/\bar{M}_n = 1.39$. This data suggests that the PEDOT-Bu-Phos is slightly shorter than our previously reported PEDOT-Phos ($\bar{M}_n = 12\,115$ Da, $\bar{M}_w = 17\,072$ Da, and an average of 38 repeat units).[31] We also noted a very broad peak in the chromatogram graph of PEDOT-Phos corresponding to an $\bar{M}_n$ ranging from 500 to 2000 kDa, which we attribute to the aggregation of the polymer in DMF. This suggests that the PEDOT-Bu-Phos is less polar than the PEDOT-Phos, as will be expected from extending the alkyl spacer.

We used attenuated total reflectance Fourier transform infrared (ATR-FTIR) spectroscopy to confirm the functionalization of PEDOT-Bu-Phos with phosphonate groups (Figure S20A, Supporting Information). Here the phosphonate P=O stretch was observed at 1175 cm^{-1} and phosphonate P-O stretching modes were visible at 1067 cm^{-1} and 1005 cm^{-1}. Raman spectroscopy (Figure S20B, Supporting Information) confirmed the presence of the PEDOT backbone as we observed moderately strong peaks in the region 2800–3000 cm^{-1} for alkyl C-H stretching in the side chain and ethylenedioxy bridge, as well as very strong peaks in the region 1350–1600 cm^{-1} from the thiophene-based backbone. The peaks from ATR-FTIR and Raman spectroscopy are assigned in Table S1, Supporting Information. X-ray photoelectron spectroscopy (XPS) provided further confirmation of the chemical structure of PEDOT-Bu-Phos as shown in the Supporting Information (Figure S20C–F, Supporting Information).

2.2. Morphological Characterization

We used grazing-incidence wide-angle X-ray scattering (GI-WAXS) to examine the arrangement of polymer chains in films of PEDOT-Phos and PEDOT-Bu-Phos. We compared films before and after cyclic voltammetry (CV) in aqueous NaCl to investigate the effect of the incorporation of hydrated ions on the morphology. The GIWAXS patterns of PEDOT-Bu-Phos exhibited some discrete in-plane and out-of-plane diffraction peaks both before and after CV, indicating an ordering of polymer chains (**Figure 1A,B**). The strong peak at $q = 2.73$ nm^{-1} ($d = 23.0$ nm) before CV shifted slightly to $q = 2.91$ nm^{-1} ($d = 21.6$ nm), with the smaller d-spacing indicating an increase in long-range ordering between crystallites caused by electrochemical cycling. The weak, in-plane scattering peaks in the region $q = 14–17$ nm^{-1} ($d = 3.7–4.5$ Å; inset of Figure 1C) further evidenced π-stacking of the conjugated backbones and packing of the alkyl side chains in ordered arrangements.[34,35] The out-of-plane scattering peak at
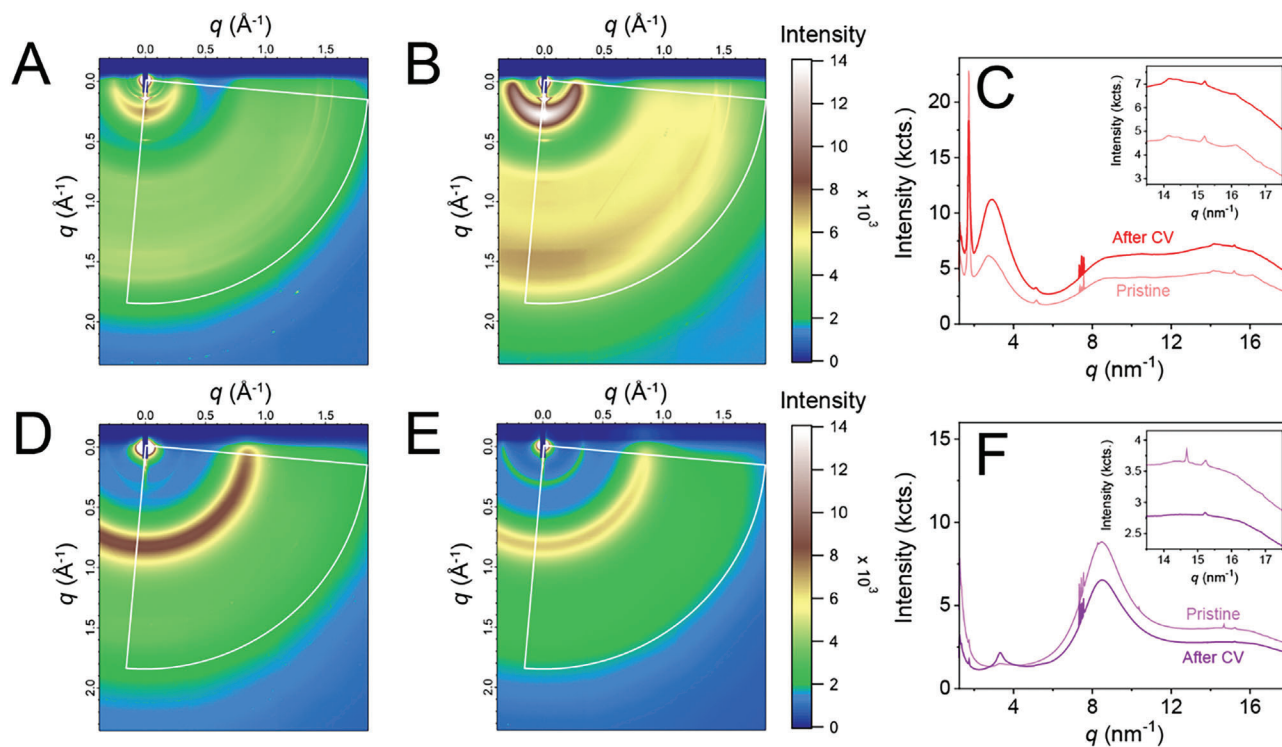
ADVANCED
SCIENCE NEWS

www.advancedsciencenews.com

ADVANCED
MATERIALS
TECHNOLOGIES

www.advmattechnol.de

Figure 1. GIWAXS of A–C) PEDOT-Bu-Phos and D–F) PEDOT-Phos films on p-doped Si(100). The left and middle columns show the raw diffraction pattern images before and after cyclic voltammetry in 0.1 M NaCl, respectively. The q-vector magnitudes displayed on the axis are the radial q-vector magnitudes from the beam center position. The right column shows the intensity versus q (radially-averaged), calculated by radial integration between the lines indicated on (A,B) and (D,E) as described in the literature.[36]

$q = 5.17$ nm^{-1} ($d = 12.1$ Å; Figure 1C) corresponded to stacking of polymer chains in the direction of the side chains.[35] This out-of-plane peak also indicated a preferential edge-on arrangement of polymer chains relative to the substrate, as has previously been observed in highly-crystalline PEDOT:PSS.[34] Nonetheless, the overall arrangement of chains in PEDOT-Bu-Phos was dominated by a lack of long-range ordering, as observed by large fractions of broad scattering. This was indicative of a paracrystalline arrangement with some ordered domains separated by regions of amorphous polymer.[35] Meanwhile, the GIWAXS patterns of PEDOT-Phos revealed a small increase in intensity of the peak at $q = 3.29$ nm^{-1} ($d = 19.1$ Å) after CV (Figure 1F), indicating a slight increase in long-range ordering of adjacent crystallites. Besides this change, however, we observed only amorphous halos (Figure 1D,E) and very weak peaks in the region $q = 14–17$ nm^{-1} (Figure 1F), indicating a highly isotropic arrangement of chains and low degree of structural order in this polymer, both before and after CV. Table S2, Supporting Information summarizes the peak positions from GIWAXS of both polymers before and after CV. The small number of crystalline peaks visible and their low magnitude relative to the amorphous scattering, means assignment of crystallographic directions is not practical.

Although exposure of PEDOT-Bu-Phos and PEDOT-Phos films to an aqueous electrolyte during CV had little impact on the chain packing seen in GIWAXS, at the meso-scale we observed changes in both polymer film's surface morphology caused by

ion diffusion from an aqueous medium. We observed these changes in topography and phase plots acquired using atomic force microscopy (AFM). The phase plots provide information on the local rigidity, and hence crystallinity, of the samples' microstructures; large phase angles correspond to more rigid, crystalline regions on the surface, while smaller phase angles indicate softer, more amorphous regions.[37] The topography of the dry films exhibited some surface pores (**Figure 2**A,G) and the phase angles showed low contrast across the whole surface (Figure 2B,C,H,I), demonstrating that there was little formation of discrete crystalline domains and the variations in phase were more indicative of local differences in film topography. This absence of ordered regions is in agreement with the limited long-range crystalline ordering observed in GIWAXS. When the films were immersed in phosphate buffered saline (PBS) solution, hydrated ions diffused into the polymer and caused the topography to change to exhibit some isolated regions of more crystalline polymer, seen as bright regions in the phase images. The phase contrast also increased indicating the rearrangement of the polymer into separate, ordered, and disordered regions (Figure 2D–F,J–L). The changes upon exposure to electrolyte were especially prominent for PEDOT-Bu-Phos, where the film began to separate into more rigid, crystalline layers surrounded by softer, more amorphous material (Figure 2D–F). This substantial change in the morphology of PEDOT-Bu-Phos was reflected in the large increase in root-mean-square surface roughness from $S_q = 5.4$ nm (dry) to $S_q = 143.5$ nm (wet). In

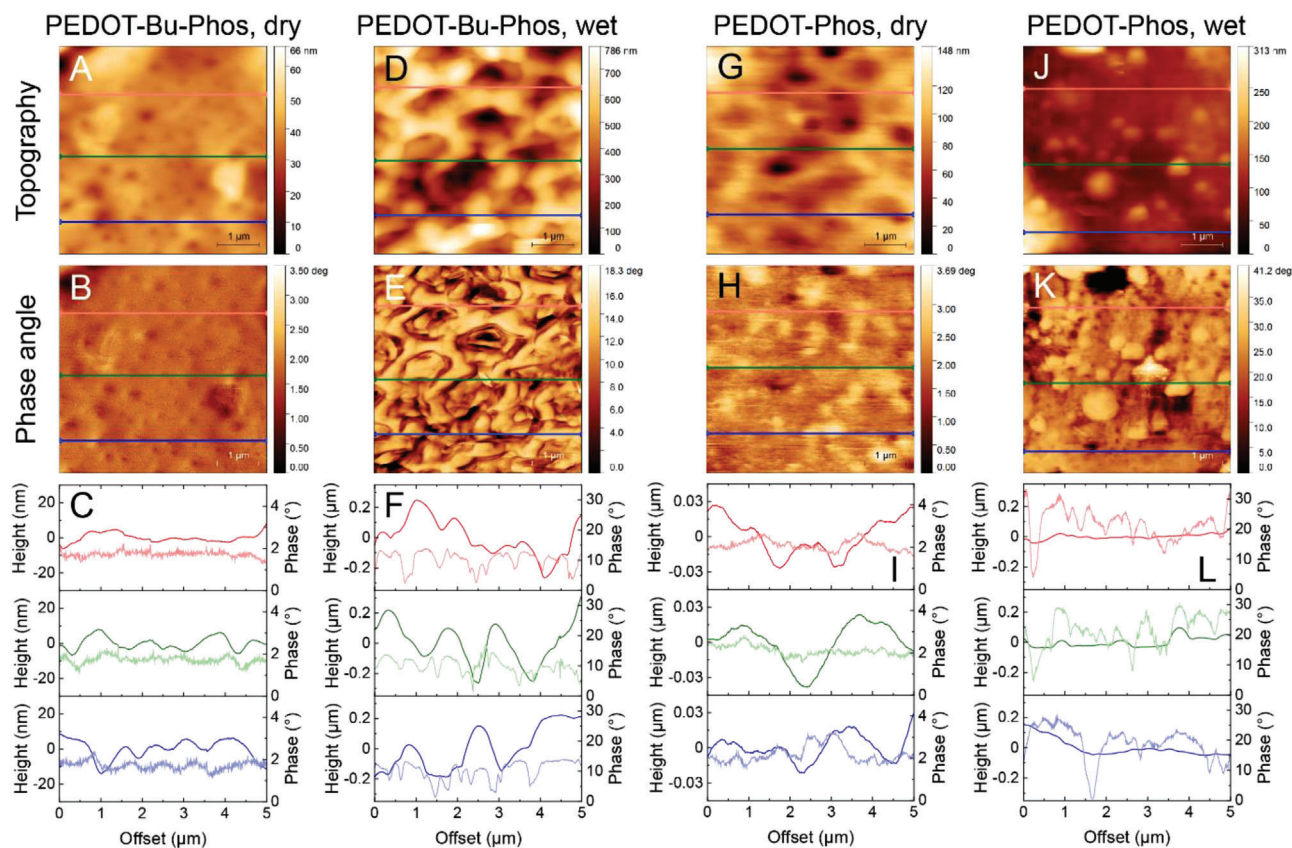**Figure 2.** AFM topography and phase micrographs (5 µm × 5 µm) and profiles of PEDOT-Bu-Phos films in A–C) dry and (D–F) wet conditions, and of PEDOT-Phos films in G–I) dry and J–L) wet conditions. The profiles show the topography (dark lines) and phase angle (pale lines) along the three horizontal lines on the micrographs.

contrast, PEDOT-Phos underwent only a small increase in roughness from S_q = 18.6 nm (dry) to S_q = 38.0 nm (wet). Thus, the phenomenon of disconnected ordered regions separated by amorphous material in PEDOT-Bu-Phos was observed in both GIWAXS and AFM.

We performed heat-flux differential scanning calorimetry (DSC) to characterize the thermal transitions in our phosphonated PEDOTs. PEDOT-Bu-Phos exhibited a small endothermic peak at 174.6 °C, possibly corresponding to melting of alkyl side chains in an ordered arrangement, and a much stronger endothermic peak at 269.0 °C corresponding to melting of crystalline, π-stacked polymer chains (Figure S21A, Supporting Information). However, PEDOT-Phos also exhibited a small melting peak at 248.1 °C (Figure S21B, Supporting Information), indicating a low degree of ordering in the film, despite the fact that no ordering was observed in the GIWAXS patterns (Figure 1D,E). This mismatch between GIWAXS and DSC has been highlighted for the conjugated polymer poly[N-9′-heptadecanyl-2,7-carbazole-alt-5,5-(4′,7′-di-2-thienyl-2′,1′,3′-benzothiadiazole)][35] and demonstrates that the highly-amorphous PEDOT-Phos underwent only limited ordering which was not readily detected using GIWAXS. Importantly, we did not observe a glass transition for either polymer, which is typical of paracrystalline conjugated polymers, in agreement with the GIWAXS results.[35]

2.3. Optical and Electrochemical Characterization

We compared the ultraviolet-visible light-near infrared (UV–vis-NIR) absorption spectra of solutions and films of PEDOT-Bu-Phos (**Figure 3**A) and PEDOT-Phos (Figure 3B). The spectra exhibited a prominent π–π* transition band in the range 560–590 nm. This band became red-shifted by around 20 nm upon the transition from solution to film due to the closer arrangement and packing of polymers in the solid state. The films also exhibited several vibronic shoulders, indicating the presence of some highly-ordered regions of π-stacked polymer chains in the film.[38,39] This is in agreement with the results from DSC which revealed the presence of crystalline aggregates in the films. The Tauc plot of the PEDOT-Bu-Phos film (Figure S22A, Supporting Information) yielded an optical bandgap energy of $E_{g,opt}$ = 1.76 eV, which was slightly narrower than for PEDOT-Phos with $E_{g,opt}$ = 1.80 eV.[31] CV of PEDOT-Bu-Phos in aqueous NaCl revealed clear electrochemical oxidation and reduction waves (Figure 3C), demonstrating the polymer's electrochemical activity in an aqueous electrolyte. The peak current density was proportional to the scan rate, indicating that redox was controlled by charge carrier transport and not limited by the diffusion of counterions.[40] We also observed the electrochemical switching of PEDOT-Bu-Phos using in situ UV–vis-NIR spectroelectrochemistry in aqueous NaCl. As the applied
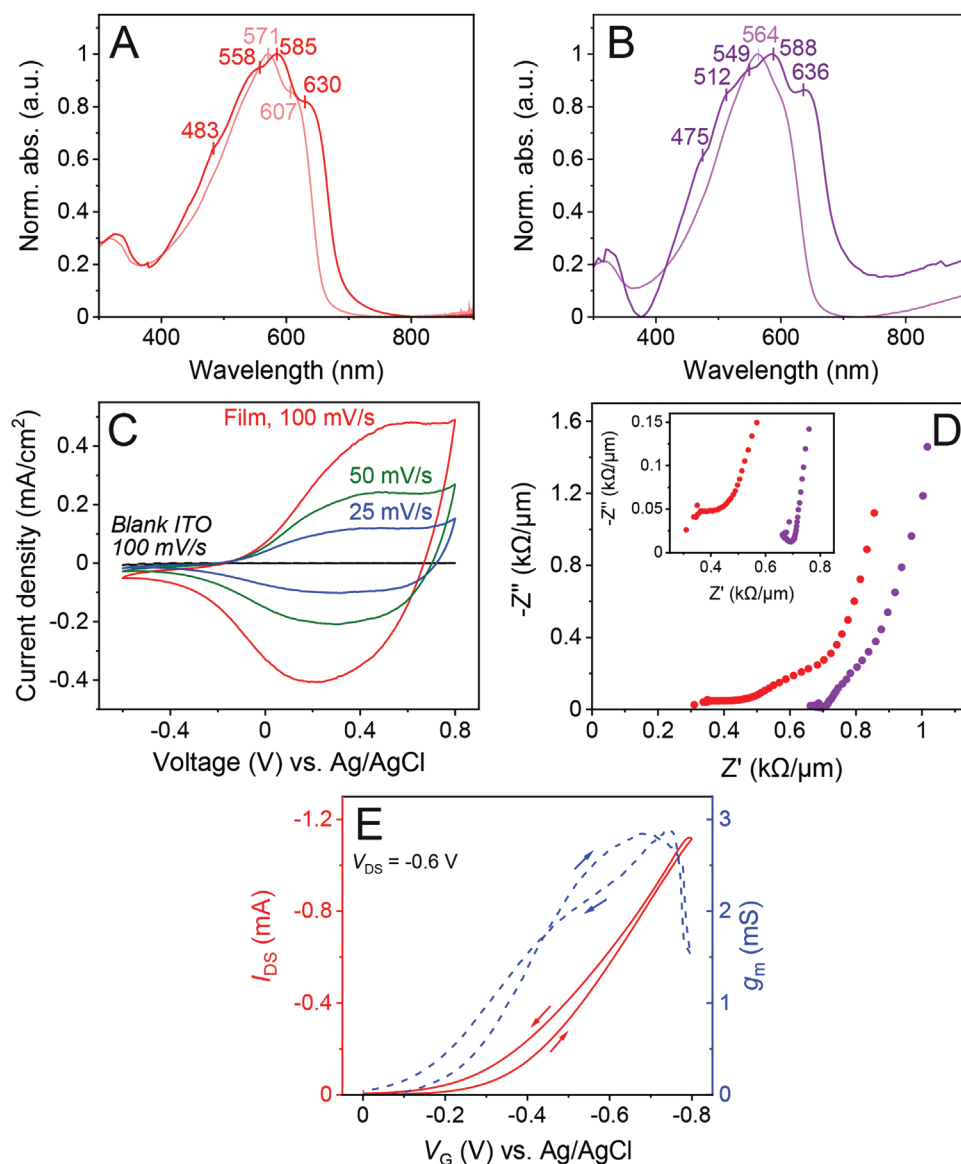
Figure 3. Optical, electronic, and OECT characterization of PEDOT-Bu-Phos. A,B) UV–vis-NIR spectra of solutions in $CHCl_3$ (pale lines) and films on ITO (dark lines) of A) PEDOT-Bu-Phos; B) PEDOT-Phos; Adapted with permission.[31] Copyright 2022, American Chemical Society. C) Cyclic voltammetry of PEDOT-Bu-Phos on ITO in 0.1 M NaCl at various scan rates. D) Nyquist plots of PEDOT-Bu-Phos (red) and PEDOT-Phos (purple) in 0.1 M NaCl at an applied potential of +0.4 V. The inset shows detail of the high-frequency impedance data. E) Transfer curve (red) and transconductance (blue) of a representative PEDOT-Bu-Phos OECT in 0.1 M NaCl.

potential was increased, the $\pi-\pi^*$ transition band decreased in intensity and polaron and bipolaron charge carrier bands appeared in the infrared region (Figure S23A, Supporting Information). These polaron and bipolaron bands first appeared at mild applied potentials of −0.44 V and −0.14 V vs Ag/AgCl respectively, highlighting that PEDOT-Bu-Phos can undergo electrochemical switching at low potentials. The spectroelectrochemical changes were also reversible, seen as the charge carrier bands progressively disappeared and the $\pi-\pi^*$ band was restored as the polymer was reduced (Figure S23B, Supporting Information). We also performed in situ double-step spectrochronoamperometry to demonstrate the reversibility and good stability of electrochromic switching, since films of PEDOT-Bu-Phos retained up to 83% of their optical contrast after nearly

20 min of continuous cycling between oxidized and reduced states (Figure S23C, Supporting Information). From the cyclic voltammograms, the oxidation onset of PEDOT-Bu-Phos was −0.047 V vs Ag/AgCl (Figure S22B, Supporting Information). This potential was slightly higher than that of PEDOT-Phos (−0.157 V vs Ag/AgCl), corresponding to a higher energy requirement for electrochemical switching in the aqueous electrolyte, which arose since the longer hydrophobic butyl spacer decreased the polymer's affinity to hydrated counterions. However, this oxidation onset potential was still close to zero, demonstrating the electrochemical activity of both our phosphonated PEDOTs at mild voltages, and thereby, their potential application for energy-efficient devices. From the optical bandgap energy and the oxidation onset potential in CV, we also calculated

the energies of the highest occupied (E_{HOMO} = −4.85 eV) and lowest unoccupied (E_{LUMO} = −3.09 eV) molecular orbitals and the IP (IP = 4.85 eV). This IP was slightly higher than that of PEDOT-Phos (IP = 4.74 eV), as expected from the higher oxidation onset potential. **Table 1** summarizes and compares the optical and electronic properties of both polymers.

We obtained the Nyquist plots of PEDOT-Phos and PEDOT-Bu-Phos at an applied potential of +0.4 V (Figure 3D). The Nyquist plots exhibited two regimes: a high-frequency semicircle with radius proportional to the resistance to charge transfer, and a low-frequency diffusive tail indicating a mixed capacitance-impedance response, similar to the behavior of PEDOT-Phos.[31] Comparing the two polymers, the radius of the high-frequency semicircle was larger for PEDOT-Bu-Phos, corresponding to a larger charge transfer resistance. Furthermore, the slope of the diffusive tail was less steep for PEDOT-Bu-Phos at low frequencies. These features demonstrate that the diffusion of hydrated counterions was slower into the PEDOT-Bu-Phos film due to the longer hydrophobic spacer.[41] Bode impedance and phase plots similarly revealed that the polymer decreased in impedance and underwent a change from capacitive to resistive behavior as it was progressively oxidized (Figure S22C,D, Supporting Information).

We complemented these results with density functional theory (DFT) calculations of PEDOT-Bu-Phos single molecules and crystalline solids, with the relaxed geometries shown in Figures S24 and S25, Supporting Information. The theoretical IP was smaller than the experimental IP for both PEDOT-Phos and PEDOT-Bu-Phos (Figure S26A,B, Supporting Information) due to the well-known bandgap underestimation provided by semilocal DFT exchange-correlation functionals[42,43] and the use of idealized simulation conditions including a lack of solution environment. Nonetheless, the side-chain-extended PEDOT-Bu-Phos with its butylene spacer exhibited a slightly smaller bandgap energy, but also a slightly larger IP, than PEDOT-Phos with its methylene spacer, in agreement with the experimental trends. The calculated effective masses of electrons and holes close to the Fermi edge were also higher for an isolated molecule of PEDOT-Bu-Phos than PEDOT-Phos (Figure S26C, Supporting Information), which would correspond to a lower charge carrier mobility in PEDOT-Bu-Phos independent of any interactions between polymer chains.

2.4. Performance in Organic Electrochemical Transistors

We have previously demonstrated the utility of PEDOT-Phos in aqueous organic electrochemical transistors (OECTs) with high volumetric capacitances and without additives or crosslinkers.[31] As such, we also characterized the OECT performance of PEDOT-Bu-Phos, which can be related to the observed changes in morphology after contact with an aqueous electrolyte. Stand-alone films of PEDOT-Bu-Phos exhibited accumulation-mode behavior in aqueous OECTs, seen in the devices' transfer (Figure 3E) and output curves (Figure S27A, Supporting Information) as the devices were in the OFF state at zero gate potential and switched ON as a gate potential was applied. The threshold voltage of PEDOT-Bu-Phos was V_{TH} = −0.185 ± 0.008 V (Figure S27B, Supporting Information), which was only slightly larger than for PEDOT-Phos devices with V_{TH} = −0.161 ± 0.005 V,[31]

Table 1. Summary of morphological, optical, and electrochemical properties of PEDOT-Phos and PEDOT-Bu-Phos. T_m = melting temperature from DSC; λ_{max}^{soln} = wavelength of maximum optical absorption of solution; λ_{max}^{film} = wavelength of maximum optical absorption of film; $V_{ox,onset}$ = oxidation onset potential in CV; E_g = bandgap energy; E_{HOMO} = energy of highest-occupied molecular orbital; E_{LUMO} = energy of lowest-unoccupied molecular orbital; IP = ionization potential. E_{HOMO} and E_{LUMO} are reported relative to the vacuum energy, E_{vac} = 0 eV. The values reported for the DFT method are for isolated molecules. E_{HOMO} was calculated from E_{LUMO} using a bandgap energy of 2 × E_g as described in the Experimental Section. The experimental bandgap is the optical bandgap, $E_{g,opt}$, calculated using UV–vis–NIR spectroscopy.

Method	Polymer	T_m [°C]	λ_{max}^{soln} [nm]	λ_{max}^{film} [nm]	$V_{ox,onset}$ (V vs Ag/AgCl)	E_g [eV]	E_{HOMO} [eV]	E_{LUMO} [eV]	IP [eV]
Experimental	PEDOT-Phos	248.1	564a)	588a)	−0.157a)	1.80a)	−4.74a)	−2.95a)	4.74a)
	PEDOT-Bu-Phos	173.2/269.5	571	585	−0.047	1.76	−4.85	−3.09	4.85
DFT	PEDOT-Phos	—b)	—b)	—b)	—b)	0.89a)	−4.05a)	−2.27a)	4.05a)
	PEDOT-Bu-Phos	—b)	—b)	—b)	—b)	0.88	−4.21	−2.44	4.21

a) Experimental values for PEDOT-Phos: Reproduced with permission.[31] Copyright 2022, American Chemical Society. b) Not measured.

**ADVANCED
SCIENCE NEWS**

www.advancedsciencenews.com

**ADVANCED
MATERIALS
TECHNOLOGIES**

www.advmattechnol.de

consistent with the slightly higher IP of PEDOT-Bu-Phos. However, side chain extension resulted in a fourfold decrease in the maximum transconductance ($g_{m,max} = 2.3 \pm 0.6$ mS at $V_{G,max} = -0.63 \pm 0.17$ V) and the ON/OFF current ratio ($I_{ON}/I_{OFF} = 165 \pm 58$). Normalized to the thickness, the maximum g_m of PEDOT-Phos ($g_{m,max}/d = 160 \pm 32$ S cm^{-1}) was twelve times higher than that of PEDOT-Bu-Phos ($g_{m,max}/d = 13.2 \pm 1.8$ S cm^{-1}). This lower device response likely arose since hydrated counterions gather around the polar phosphonate groups[32,33] but must still compensate the charge carriers in the conjugated backbone. Since in PEDOT-Bu-Phos the counterions and phosphonate groups are separated from the backbone by the longer butylene spacer, the counterions are less effective in compensating the charge carriers in the backbone and so fewer charge carriers can be supported. In contrast, the short methylene spacer in PEDOT-Phos allows the counterions to accumulate close to the conjugated backbone, facilitating the compensation of charge carriers and enhancing the electrochemical response.

Using electrochemical impedance spectroscopy (EIS), we calculated the capacitance for our devices as a function of frequency (Figure S27C, Supporting Information). From this data, the volumetric capacitance of PEDOT-Bu-Phos reached a maximum value of $C^* = 49 \pm 5$ F cm^{-3} at +0.4 V. This C^* was larger than that of PEDOT:PSS treated with ethylene glycol ($C^* = 39 \pm 3$ F cm^{-3}),[44] as well as PEDOT functionalized with carboxylic acid groups ($C^* = 36 \pm 3$ F cm^{-3}).[41] However, it was lower than the C^* of PEDOT-Phos with a shorter methylene spacer ($C^* = 282 \pm 62$ F cm^{-3}) (Table S3, Supporting Information).[31] The lower C^* of PEDOT-Bu-Phos, as well as the higher IP and oxidation onset potential discussed above, further indicates a lower uptake of hydrated counterions by PEDOT-Bu-Phos. This in turn was caused by the increase in ordering and aggregation of PEDOT-Bu-Phos chains, as seen in GIWAXS, and the increased hydrophobicity of the polymer due to the longer alkyl spacer. This improved ordering of the polymer chains in PEDOT-Bu-Phos would be expected to result in a decreased C^*, but also should improve the intermolecular charge transport and electronic properties.[45] However, this charge transport also requires sufficiently long chains to bridge ordered domains, but the short chains of PEDOT-Bu-Phos observed in GPC suggested a low degree of interconnection, contributing to the low charge carrier mobility and transconductance. Additionally, we postulate that once the hydrated ions entered the PEDOT-Bu-Phos film, they separated more crystalline regions from each other as we observed in AFM,[27] further hindering intermolecular charge transport through the film which resulted in a lower transconductance. Nonetheless, the performance of our OECTs is strongly dependent on the diffusion of ions into the entire channel volume, which also changes the polymer's morphology and electrochemistry.[27] Different device architectures such as organic field-effect transistors would eliminate the effect of hydration and may give rise to different properties of our phosphonated PEDOTs.

Side chain engineering of conjugated polymers has been employed to control the properties of the active channel in OECTs.[7] The hydrophilicity/hydrophobicity of the side chain has been shown to be a critical factor in modulating the ion uptake and its stabilization in the film. A more hydrophilic side chain results in active swelling of the channel, improving its volumetric capacitance and transconductance.[24,26,28,29,46–48] We observed a similar effect with our phosphonate functionalized PEDOT polymers.

The polar phosphonate group in PEDOT-Bu-Phos is separated by a butyl spacer from the backbone, increasing its hydrophobicity in comparison to PEDOT-Phos that has the phosphonate group spaced from the backbone by one methylene group. We speculate that this increased hydrophobicity resulted in a decrease in the uptake of hydrated ions, seen by the increase in the IP and the threshold voltage, and the decrease in the volumetric capacitance of PEDOT-Bu-Phos. Another critical factor that governs the performance of the OECT is the microstructure of the active channel. Mobility increases in films having well-connected long-range crystalline domains where swelling does not interrupt the conduction pathway between the crystalline regions.[34] However, mobility has also been shown to decrease for films with increased crystallinity.[27,49] This trend was attributed to low molecular weight polymers that form small-size crystallites in different orientations, impeding charge transport in between.[50] In agreement with these findings, our phosphonated PEDOTs had similar, low molecular weights and correspondingly low mobilities. The improved chain packing of PEDOT-Bu-Phos in crystallites also limited the interconnectivity between crystallites, further decreasing its mobility compared to PEDOT-Phos with similar molecular weight but minimal ordering.

3. Conclusions

Conjugated polymers are attractive due to their mixed ionic-electronic conductivity, but this property also represents a synthetic challenge, since it requires both the ionic and electronic transport properties to be optimized simultaneously. In our previous work, the importance of ionic conductivity was seen with the high volumetric capacitance C^* of PEDOT-Phos having the phosphonate group in close proximity to the backbone, allowing ions to diffuse into the film to accumulate close to the conjugated backbone. In this work, we synthesized phosphonated PEDOT with an extended butyl spacer to investigate the effect of side chain extension on the polymer's morphological and electrochemical properties.

Extending the spacer resulted in improved packing and ordering, seen in the emergence of paracrystalline ordering in GIWAXS and DSC. While this improved packing should have improved the electronic charge transport within paracrystalline domains, this was not the case. Instead, the butylene spacer increased the polymer's hydrophobicity and likely prevented the diffusion of ions close to the backbone to compensate charge carriers, resulting in a diminished electrochemical response. This was reflected in the decreased volumetric capacitance and higher threshold voltage seen in the OECT device. Furthermore, changes in the film's topography indicated that hydration of the film might have disrupted the paracrystalline domains observed in PEDOT-Bu-Phos. Well-interconnected ordered domains are required for good bulk electronic conductivity before and after exposure to the electrolyte. This may be achieved using a polar, alkoxy spacer instead of a hydrophobic alkyl spacer. On the other hand, utilizing these phosphonated PEDOTs in organic field effect transistors would not require hydration and may allow us to exploit these polymers' energy-efficient switching in films with an improved morphology and uninterrupted inter-domain connectivity. Our results emphasize that fine-tuning the balance between ionic conductivity and long-range molecular ordering is critical to optimize the synthetic design of conjugated polymers.

**ADVANCED
SCIENCE NEWS**

www.advancedsciencenews.com

**ADVANCED
MATERIALS
TECHNOLOGIES**

www.advmattechnol.de

4. Experimental Section

Materials: 3,4-dimethoxythiophene (3,4-DMT, 95%) was purchased from AK Scientific. *p*-Toluenesulfonyl chloride (TosCl) and 4-dimethylaminopyridine (DMAP) were purchased from Arcos Organics and used as received. Deuterated chloroform (CDCl3) was obtained from Cambridge Isotope Laboratories. Sodium hydroxide pellets (NaOH) and sodium hydrogen carbonate (NaHCO3) were obtained from Univar. Toluene (ChemSupply) was dried over molecular sieve absorbent beads (3 Å, 8–12 mesh, Sigma-Aldrich) and stored under nitrogen. All other chemicals were obtained from Sigma-Aldrich or ChemSupply and used as received. For column chromatography, chromatographic silica media LC60A (40–63 micron) and thin layer chromatographic silica gel 60 F254 plates (Merck) with dimensions 20 × 20 cm and no fluorescent indicator were purchased from Sigma-Aldrich, and acid-washed sand (grain size ≈300–350 μm) was obtained from ChemSupply. The synthesis of PEDOT-Phos was conducted as described in ref. [31]

Synthesis of 4-(2,3-Dihydrothieno[3,4-b][1,4]Dioxin-2-yl) Butan-1-ol (EDOT-Bu-OH): 3,4-DMT (466.8 mg, 3.24 mmol) was dissolved in anhydrous toluene (17 mL) in a round-bottom flask under a nitrogen atmosphere. 1,2,6-hexanetriol (0.78 mL, 6.48 mmol, 2 mol. equiv.) and anhydrous $NaHSO_4$ (272.1 mg, 2.27 mmol, 0.7 mol. equiv.) were added and the reaction mixture was refluxed at 110 °C with vigorous stirring under nitrogen for 24 h. Reaction progress was monitored using thin-layer chromatography. The reaction mixture was decanted into a separatory funnel and the yellow organic fraction was washed twice with aqueous $NaHCO_3$ solution (5 w/w%), then once with aqueous saturated sodium chloride (NaCl) solution. The organic layer was dried with solid $MgSO_4$, then filtered and solvent was removed by rotary evaporation. The crude product was further purified using flash column chromatography with ethyl acetate (EtOAc):triethylamine (TEA):*n*-hexane (29:1:70 v/v%) initially, then EtOAc:TEA (99:1 v/v%) used as eluent. The product EDOT-Bu-OH (82.0 mg, 12 mol%) was obtained as a golden oil and analyzed by ^{1}H-NMR (400 MHz, CDCl$_3$, δ) (ppm): 6.30 & 6.30 (dd, 2H, thiophene CH), 4.16 & 3.87 (dd, 2H, ethylenedioxy CH$_2$), 4.13 (m, 1H, ethylenedioxy CH), 3.68 (t, 2H, butyl C$\underline{H}_2$OH), 1.63 (m, 6H, butyl C$\underline{H}_2$CH$_2$), 1.36 (s, 1H, alcohol OH). ^{13}C NMR (100 MHz, CDCl$_3$, δ): 142.1 & 141.7 (thiophene β-C), 99.4 & 99.3 (thiophene α-C), 73.7 (ethylenedioxy CH), 68.4 (ethylenedioxy CH$_2$), 62.6 (butyl C$\underline{H}_2$OH), 32.4 (butyl CH$_2$CH$_2$$\underline{C}H_2CH_2$OH), 30.4 (butyl $\underline{C}$H$_2$CH$_2$CH$_2$$\underline{C}H_2$OH), 21.4 (butyl CH$_2$$\underline{C}H_2CH_2CH_2$OH).

Synthesis of 4-(2,3-Dihydrothieno[3,4-b][1,4]Dioxin-2-yl) Butyl 4-Methylbenzenesulfonate (EDOT-Bu-Tos): EDOT-Bu-OH (123.4 mg, 0.576 mmol) was dissolved in anhydrous CHCl$_3$ in a round-bottom flask under nitrogen. *p*-toluenesulfonyl chloride (TosCl, 219.6 mg, 1.15 mmol, 2 mol. equiv.), TEA (0.22 mL, 1.61 mmol, 2.8 mol. equiv.), and *N,N*-dimethylaminopyridine (14.1 mg, 0.116 mmol, 0.2 mol. equiv.) were added sequentially. The mixture was stirred at room temperature for 3 h, then a 10 v/v% aqueous solution of sulfuric acid (H$_2$SO$_4$, 2 mL) and saturated aqueous NaHCO$_3$ solution (4 mL) were added dropwise. The organic layer was washed three times with saturated aqueous NaHCO$_3$ solution, dried over anhydrous MgSO$_4$, and solvent was removed by rotary evaporation. The product, EDOT-Bu-Tos (210.0 mg, 99%) was obtained as a golden-brown oil. ^{1}H-NMR (400 MHz, CDCl$_3$, δ) (ppm): 7.79 (d, 2H, tosyl ArH), 7.34 (d, 2H, tosyl ArH), 6.30 & 6.28 (dd, 2H, thiophene CH), 4.11 (dd, 1H, ethylenedioxy CH$_2$), 4.06 (t, 1H, ethylenedioxy CH), 4.04 (m, 2H, butyl CH$_2$CH$_2$CH$_2$$\underline{C}H_2$OTos), 3.82 (dd, 1H, ethylenedioxy CH$_2$), 2.46 (s, 3H, tosyl CH$_3$), 1.72 (m, 2H, butyl C$\underline{H}_2$CH$_2$CH$_2$CH$_2$OTos), 1.64 & 1.56 (m, 2H, butyl CH$_2$$\underline{C}H_2CH_2CH_2$OTos), 1.60 & 1.50 (m, 2H, butyl CH$_2$C$\underline{H}_2$CH$_2$CH$_2$OTos). ^{13}C NMR (100 MHz, CDCl$_3$, δ): 144.8 (tosyl aromatic SO$_2$−$\underline{C}$−(CH)$_2$), 141.9 & 141.6 (thiophene β-C), 133.1 (tosyl aromatic (CH)$_2$−$\underline{C}$−CH$_3$), 129.9 & 129.8 (tosyl aromatic ($\underline{C}$-H)$_2$CCH$_3$), 127.9 & 127.9 (tosyl aromatic SO$_2$C-($\underline{C}$-H)$_2$), 99.4 (thiophene α-C), 73.3 (ethylenedioxy CH), 70.1 (butyl $\underline{C}$H$_2$CH$_2$CH$_2$CH$_2$OTos), 68.2 (ethylenedioxy CH$_2$), 29.9 (butyl CH$_2$$\underline{C}H_2CH_2CH_2$OTos), 28.7 (butyl CH$_2CH_2$$\underline{C}H_2CH_2$OTos), 21.6 (tosyl C$\underline{H}_3$), 21.1 (butyl CH$_2$$\underline{C}H_2CH_2CH_2$OTos).

Synthesis of 4-(2,3-Dihydrothieno[3,4-b][1,4]Dioxin-2-yl) 1-Iodobutane (EDOT-Bu-I): EDOT-Bu-Tos (210.0 mg, 0.570 mmol) was dissolved in acetone (1.8 mL) in a round-bottom flask under nitrogen and sodium iodide (NaI, 863.4 mg, 5.76 mmol, 10 mol. equiv.) was added. The mixture was refluxed at 60 °C for 18 h, after which acetone was removed by rotary evaporation. Finally, the crude product was purified by flash column chromatography with EtOAc:TEA:*n*-hexane (29:1:70 v/v%) and was then EtOAc:TEA (99:1 v/v%) used as eluent. The product, EDOT-Bu-I (183.0 mg, 98%) was obtained as an orange oil. ^{1}H-NMR (400 MHz, CDCl$_3$, δ) (ppm): 6.30 (dd, 2H, thiophene CH), 4.16 & 3.88 (dd, 2H, ethylenedioxy CH$_2$), 4.12 (m, 1H, ethylenedioxy CH), 3.21 (t, 2H, butyl C$\underline{H}_2$I), 1.89 (m, 2H, butyl CH$_2$CH$_2$$\underline{C}H_2CH_2$I), 1.69 & 1.61 (m, 4H, butyl C$\underline{H}_2$CH$_2$CH$_2$CH$_2$I and butyl CH$_2$C$\underline{H}_2$CH$_2$CH$_2$I). ^{13}C NMR (100 MHz, CDCl$_3$, δ): 141.9 & 141.6 (thiophene β-C), 99.5 & 99.4 (thiophene α-C), 73.4 (ethylenedioxy CH), 68.3 (ethylenedioxy CH$_2$), 33.1 (butyl CH$_2$$\underline{C}H_2CH_2CH_2$I), 29.5 (butyl CH$_2CH_2$$\underline{C}H_2CH_2$I), 26.0 (butyl CH$_2CH_2CH_2$$\underline{C}H_2$I), 6.2 (butyl CH$_2CH_2CH_2C\underline{H}_2$I).

Synthesis of Diisopropyl (4-(2,3-Dihydrothieno[3,4-b][1,4]Dioxin-2-yl) Butyl) Phosphonate (EDOT-Bu-Phos): EDOT-Bu-I (183.0 mg, 0.564 mmol) was dissolved in anhydrous toluene (2 mL) in a round-bottom flask under nitrogen and triisopropylphosphite (P(O*i*-Pr)$_3$, 0.28 mL, 1.13 mmol, 2 mol. equiv.) was added. The mixture was refluxed at 120 °C under nitrogen for 48 h, with aliquots of P(O*i*-Pr)$_3$ (0.14 mL, 0.564 mmol, 1 mol. equiv.) added to the reaction mixture at 8, 24, and 32 h. After 48 h, toluene was removed by rotary evaporation and the product was purified by flash column chromatography with EtOAc:TEA:*n*-hexane (29:1:70 v/v%) then EtOAc:TEA (99:1 v/v%) used as eluent. The product, EDOT-Bu-Phos (130.8 mg, 64%) was obtained as a yellow oil and analyzed by ^{1}H-NMR (400 MHz, CDCl$_3$, δ) (ppm): 6.30 & 6.28 (dd, 2H, thiophene CH), 4.68 (m, 2H, J_{HP} = 8.0 Hz, isopropyl CH), 4.13 & 3.86 (dd, 2H, ethylenedioxy CH$_2$), 4.10 (m, 1H, ethylenedioxy CH), 1.62 (m, 8H, butyl CH$_2$), 1.30 ppm (m, 12H, isopropyl CH$_3$). ^{13}C NMR (100 MHz, CDCl$_3$, δ): 142.0 & 141.6 (thiophene β-C), 99.4 & 99.3 (thiophene α-C), 73.5 (ethylenedioxy CH), 70.0 & 69.8 (isopropyl CH), 68.4 (ethylenedioxy CH$_2$), 30.2 (butyl CH$_2$CH$_2$CH$_2$$\underline{C}H_2$P), 27.6 (butyl $\underline{C}$H$_2$CH$_2$CH$_2$CH$_2$P), 26.2 & 26.1 & 25.9 (butyl CH$_2$$\underline{C}H_2CH_2CH_2$P), 24.1 ($J_{CP}$ = 6.6 Hz, isopropyl CH$_3$), 22.7 & 22.6 (butyl CH$_2$CH$_2$$\underline{C}H_2CH_2$P). ^{31}P NMR (162 MHz, CDCl$_3$) δ: 29.8 (phosphonate P).

Synthesis of PEDOT-Bu-Phos: Powdered iron(III) chloride (FeCl$_3$, 274.9 mg, 1.69 mmol) was dispersed in anhydrous chloroform (5.9 mL) under nitrogen. EDOT-Bu-Phos (147.9 mg, 0.408 mmol) was dissolved in anhydrous chloroform (1.1 mL) in a separate vial. This monomer solution was then added dropwise to the reaction flask and the mixture was stirred for 24 h at room temperature. The mixture was then poured into excess methanol and centrifuged at 7000 rpm for 5 min; the supernatant was then decanted off. The remaining solid product was washed and centrifuged, four times with methanol and twice with deionized water, then freeze-dried. The product, oxidized PEDOT-Bu-Phos (81.3 mg, 62%) was obtained as a flaky black powder. To reduce this oxidized polymer, oxidized PEDOT-Bu-Phos (20.0 mg) was dispersed in CHCl$_3$ (4 mL) in a glass vial and hydrazine monohydrate (4 drops) was added. The mixture was stirred overnight at room temperature, then decanted into a separatory funnel and washed three times with deionized water. The purple organic layer was collected, and solvent was removed by rotary evaporation. The product, PEDOT-Bu-Phos, was finally obtained as a dark purple solid.

Fabrication of Polymer Films: Polymer solutions were prepared by dissolving PEDOT-Phos in CHCl$_3$ (5.0 mg mL^{-1}) at room temperature. Before fabricating the film, indium tin oxide (ITO)-coated glass substrates and p-doped silicon (100) substrates were cleaned by immersion in basic piranha solution at 60 °C for 15 min, then rinsed with deionized water and acetone and dried under a flow of nitrogen gas. Films were then produced by drop-casting the solutions onto the substrates and leaving them to dry at room temperature. For AFM, CV, GIWAXS, and XPS, the polymer solution (20 μL) was drop-cast onto an area of 8 mm × 5 mm for AFM, CV, and GIWAXS, or 8 mm × 8 mm for XPS. For in situ UV–vis-NIR spectroelectrochemistry, the solution (40 μL) was drop-cast onto an area of dimensions 8 mm × 45 mm. For OECT measurements and EIS, the solution (10 μL) was drop-cast onto an interdigitated microelectrode (IDME)

purchased from Micrux Technologies (ED-IDE1-Au) with channel width W = 50 cm and channel length L = 10 μm. The thickness of each film was measured using a Dektak IIA profilometer with tilt correction.

Structural Characterization: Solution nuclear magnetic resonance (NMR) spectroscopy was performed using a Bruker Avance III 400 spectrometer (400.14 MHz, ^{1}H; 100.62 MHz, ^{13}C; 161.97 MHz, ^{31}P) with a 5 mm BBFO probe. Samples were analyzed at 298 K in CDCl$_3$ filtered through anhydrous solid K$_2$CO$_3$ directly before use. All chemical shifts were stated in ppm (δ) relative to tetramethylsilane (δ = 0), referenced to the chemical shifts of residual solvent resonances (^{1}H, δ_H 7.26 and ^{13}C, δ_C 77.0). Coupling constants (J) were reported in Hz and multiplicities were denoted as singlet (s), doublet (d), triplet (t), quartet (q), or multiplet (m). ^{31}P spectra were calibrated to H$_3$PO$_4$ (85%) (δ_P = 0). NMR spectra were processed using Bruker TopSpin 4.1.0 software.

Gel permeation chromatography was performed using an LC20A HPLC system (Shimadzu). The column was a Styragel HT4 column (Waters, WAT044511) with particle size of 10 μm, inner diameter of 7.8 mm, and length of 300 mm. A refractive index detector (RID-10A) and a photodiode array detector (SPD-M20A) were used for detection. The sample was eluted in DMF at 30 °C and a flow rate of 1 mL min^{-1}. Calibration was performed to polystyrene standards ranging from 1320 to 3 040 000 Da. The chromatograms were processed using Shimadzu LC solution software.

Fourier-transform infrared spectroscopy (FTIR) of drop-cast films on glass/ITO substrates was conducted using a Spectrum Two FTIR spectrometer (Perkin Elmer) operating in ATR mode. The spectra were obtained over the wavenumber range 4000–450 cm^{-1} using eight accumulations and a wavenumber resolution of 2 cm^{-1}. Raman spectroscopy of films on glass/ITO substrates was conducted at wavelength 532 nm using a Raman microscope and spectrometer (inVia, Renishaw) calibrated against an internal silicon standard. Spectra were acquired over the wavenumber range 3200–60 cm^{-1} using four accumulations of 10 s each. XPS was performed using a Thermo ESCALAB 250 Xi X-ray photoelectron spectrometer (Thermo Scientific, UK). Samples were analyzed under high vacuum (better than 2×10^{-9} mbar) with monochromated Al-Kα (1486.68 eV) as the X-ray source from an anode operated at 120 W and a spot size of 500 μm. The spectrometer was calibrated using the Au 4f$_{7/2}$ = 83.96 eV, Ag 3d$_{5/2}$ = 368.21 eV, and Cu 2p$_{3/2}$ = 932.62 eV lines. The tube voltage was 13.8 kV, the tube current was 8.7 mA, and the pass energy was 100 eV for survey scans and 20 eV for scans of individual regions. The binding energies were referenced to the C 1s adventitious hydrocarbon peak at 284.8 eV. The peaks were deconvoluted and fitted to a mixed Gaussian-Lorentzian model using Avantage software, with the full-width half-maxima constrained to 1.0 eV for P and S and 1.2 eV for C.

Morphological Characterization: GIWAXS of films was performed at the Australian Synchrotron using a photon energy of 11.5 keV. The incident angle was 0.1° and the camera length was 660.885 mm. The data was collected using a Pilatus3-2M detector (Dectris) with a pixel size of 172 μm × 172 μm. Data were radially integrated using the software package Fit2D.[36,51] The surface topography and phase angle of PEDOT-Phos and PEDOT-Bu-Phos films were characterized using an atomic force microscope (NanoWizard II; JPK Instruments AG, Berlin, Germany). The microscope was operated in intermittent-contact mode, both in air and liquid, for imaging. PBS solution was used during aqueous imaging as the liquid medium. Images were taken with a nominal spring constant of 32 Nm^{-1} and a resonant frequency of 315 kHz using silicon cantilevers (Type ACT; AppNano, Mountain View, CA, USA). With a pixel resolution of 512 × 512, the scan rate was set to 1 Hz. Three separate 5 μm × 5 μm areas were imaged in each sample. DSC was performed using a DSC 204 F1 Phoenix (Netzsch) differential scanning calorimeter operating in heat flux mode. The sample of either PEDOT-Phos (1.19 mg) or PEDOT-Bu-Phos (0.89 mg) was drop-cast into an aluminum pan with a pierced lid. The correction and sample measurements were sequentially conducted under an argon atmosphere from −50 to +300 °C at a heating rate of 10 K min^{-1}.

Optical, Electrochemical, and Theoretical Characterization: Optical absorption spectra were recorded using a UV–vis–NIR spectrometer (Lambda 1050, PerkinElmer). Electrochemical characterization was performed in 0.1 M NaCl, with an Ag/AgCl aqueous reference electrode in 1 M potassium chloride (CHI Instruments). A Pt coil was used as the

counter-electrode. CV and EIS were performed using a potentiostat (Vertex, IVIUM). Cyclic voltammograms were obtained for various scan rates, potential ranges, and numbers of cycles. In situ UV–vis–NIR spectroelectrochemistry and double-step spectrochronoamperometry of PEDOT-Bu-Phos films were performed using a spectrophotometer (UV-1800, Shimadizu) to acquire the absorbance spectra and a potentiostat (eDAQ) controlled by EChem software to apply potential. Before obtaining spectroelectrochemistry data, each film was initially relaxed with six cycles of CV between −0.3 V to +1.1 V vs Ag wire (−0.64 V to +0.76 V vs Ag/AgCl). For spectrochronoamperometry, from 10 s onward the potential was switched between +0.8 V and −0.6 V (both vs Ag/AgCl), holding each potential for 20 s, and the absorbance at 560 nm was recorded as a function of time. The oxidation onset potential E_{ox} was obtained from the cyclic voltammograms, and the HOMO energy level and IP were estimated from E_{ox} using the equation: IP = $-E_{HOMO}$ = ($E_{ox} - E_{Fc,1/2}$ + 0.624 + 4.44) eV, where +0.624 V was the ferrocene/ferrocenium (Fc/Fc$^+$) potential in acetonitrile versus SHE[52] and +4.44 V was the absolute potential of the standard hydrogen electrode. $E_{Fc,1/2}$ was the half-wave potential of Fc/Fc$^+$ in acetonitrile, taken as the average of the oxidation and reduction peak potentials; this half-potential was measured to be +0.168 V vs Ag/Ag$^+$.

First-principles calculations based on DFT were performed using the Katana HPC cluster[53] to simulate the electrical bandgap energy, band structure, and IP of PEDOT-Phos and PEDOT-Bu-Phos data. DFT was conducted using the Vienna Ab-Initio Simulation Package[54] with projector-augmented wave potentials and an energy cut-off of 750 eV. The generalized gradient approximation to the exchange-correlation energy was that developed by Perdew et al.[55] and dispersion interactions were handled using the zero-damping DFT-D3 method of Grimme et al.[56] The following electronic states were considered as valence: C 2s and 2p; S 3s and 3p; O 2s and 2p; H 1s; P 3s and 3p. The two cases tested were an isolated chain of PEDOT-Phos (containing 78 atoms) or PEDOT-Bu-Phos (containing 96 atoms), with two repeat units in an orthorhombic unit cell (Figure S24, Supporting Information); and a crystalline solid of PEDOT-Phos (containing 156 atoms) or PEDOT-Bu-Phos (containing 192 atoms), comprising two stacked chains with two repeat units each, in a monoclinic unit cell (Figure S25, Supporting Information). In both cases, the polymer backbone repeated along the c-direction with π-stacking in the b-direction. Periodic boundary conditions were applied in all three directions. For the isolated chain, a vacuum region of roughly 30 Å was added to the simulation cell in the a- and b-directions to eliminate interchain interactions. The initial geometry was relaxed to a final force tolerance of 0.01 eV Å^{-1}, with an energy tolerance of 0.1 μeV per atom for each ionic step. A Monkhorst-Pack k-point grid of $1 \times 1 \times 6$ (isolated chain) or $2 \times 6 \times 6$ (crystalline solid) was used. Self-consistent charge densities were obtained and used to calculate the band structure via a non-self-consistent calculation with 25 k-points between various high-symmetry points in the unit cell. The effective masses of charge carriers were calculated by applying a parabolic fit to the valence and conduction band energies plotted as a function of k-point distance. The vacuum energy (E_{vac}) was extracted by calculating the local potential along one of the vacuum directions for the isolated molecule. Taking the computed LUMO energy level (E_{LUMO}) as fixed, the HOMO energy (E_{HOMO}) and IP were estimated using the equation: IP = $-E_{HOMO}$ = $E_{vac} - E_{LUMO} + 2E_g$, where E_g is the theoretical electronic bandgap energy. This theoretical E_g was multiplied by a factor of two to account for the well-known underestimation of the bandgap energy by semilocal DFT approaches.[42,43]

OECT Characterization: OECT measurements (output and transfer curves) were obtained in aqueous NaCl (0.1 M) at room temperature using a pair of Keithley 2401 source-measure units to apply the source-drain voltage V_{DS} and gate voltage V_G. I–V curves were also obtained using these source-measure units for dry pristine films drop-cast on IDMEs. The potential across the film was swept from −0.8 V to +0.8 V while measuring the current. The line of best fit was calculated, and from the slope of this line, the resistance R was then calculated using Ohm's law. From the resistance R, the conductivity σ was calculated using the equation: $\sigma = L/(R \cdot W \cdot d)$ where L, W, and d are the channel length, width, and thickness respectively.[57] The threshold voltage V_{TH} was calculated from the output curves by plotting $\sqrt{I_{DS}}$ versus V_G and extrapolating the linear

**ADVANCED
SCIENCE NEWS**

www.advancedsciencenews.com

**ADVANCED
MATERIALS
TECHNOLOGIES**

www.advmattechnol.de

portion of this curve to the x–axis.[33,58] Electrochemical impedance spectra (Bode and Nyquist plots) were obtained using a potentiostat (Vertex, IVIUM) to apply various potentials with a sinusoidal voltage oscillation of $\Delta V = 0.01$ V, at frequencies in the range 10 000–0.1 Hz. From the EIS data, the capacitance as a function of frequency was extracted using the equation: $C = 1/(2\pi f \text{Im}(Z))$.[24] The capacitance of the film at +0.4 V was obtained at 0.1 Hz and this was divided by the full film area to give the volumetric capacitance, $C*$.[40] The carrier mobility was measured using the constant gate current approach of Bernards and Malliaras.[59] Briefly, the transient I_{DS} response was recorded under a constant gate current I_G and an applied $V_{DS} = -0.1$ V, then the slope dI_{DS}/dt of this transient curve was plotted against the applied I_G. The time of flight of charge carriers τ_e was obtained as the slope of the line of best fit of the plot of dI_{DS}/dt versus I_G. Finally, the charge carrier mobility was calculated using the equation: $\mu = L^2/\tau_e V_{DS}$. For these device measurements, three devices were characterized, and the results were reported as value ± standard deviation unless otherwise specified.

Supporting Information

Supporting Information is available from the Wiley Online Library or from the author.

Acknowledgements

Conflict of Interest

The authors declare no conflict of interest.

Data Availability Statement

The data that support the findings of this study are available from the corresponding author upon reasonable request.

Keywords

[1] A. R. Murad, A. Iraqi, S. B. Aziz, S. N. Abdullah, M. A. Brza, *Polymers* **2020**, *12*, 2627.

[2] Z. Peng, K. Xian, J. Liu, Y. Zhang, X. Sun, W. Zhao, Y. Deng, X. Li, C. Yang, F. Bian, Y. Geng, L. Ye, *Adv. Mater.* **2023**, *35*, 2207884.

[3] J. W. Lee, C. Sun, B. S. Ma, H. J. Kim, C. Wang, J. M. Ryu, C. Lim, T. S. Kim, Y. H. Kim, S. K. Kwon, B. J. Kim, *Adv. Energy Mater.* **2021**, *11*, 2103234.

[4] W. T. Neo, Q. Ye, S. J. Chua, J. Xu, *J. Mater. Chem. C* **2016**, *4*, 7364.

[5] J. Kim, M. Rémond, D. Kim, H. Jang, E. Kim, *Adv. Mater. Technol.* **2020**, *5*, 1900890.

[6] S. Inal, J. Rivnay, A. O. Suiu, G. G. Malliaras, I. McCulloch, *Acc. Chem. Res.* **2018**, *51*, 1368.

[7] Y. He, N. A. Kukhta, A. Marks, C. K. Luscombe, *J. Mater. Chem. C* **2022**, *10*, 2314.

[8] S. G. Higgins, A. Lo Fiego, I. Patrick, A. Creamer, M. M. Stevens, *Adv. Mater. Technol.* **2020**, *5*, 2000384.

[9] M. Jaiswal, R. Menon, *Polym. Int.* **2006**, *55*, 1371.

[10] R. Noriega, J. Rivnay, K. Vandewal, F. P. V. Koch, N. Stingelin, P. Smith, M. F. Toney, A. Salleo, *Nat. Mater.* **2013**, *12*, 1038.

[11] C. M. Proctor, J. Rivnay, G. G. Malliaras, *J. Polym. Sci., Part B: Polym. Phys.* **2016**, *54*, 1433.

[12] X. Hu, L. Xu, *Polymer.* **2000**, *41*, 9147.

[13] T. Yamamoto, D. Komarudin, M. Arai, B. L. Lee, H. Suganuma, N. Asakawa, Y. Inoue, K. Kubota, S. Sasaki, T. Fukuda, H. Matsuda, *J. Am. Chem. Soc.* **1998**, *120*, 2047.

[14] B. Friedel, C. R. McNeill, N. C. Greenham, *Chem. Mater.* **2010**, *22*, 3389.

[15] S. Thankaraj Salammal, S. Dai, U. Pietsch, S. Grigorian, N. Koenen, U. Scherf, N. Kayunkid, M. Brinkmann, *Eur. Polym. J.* **2015**, *67*, 199.

[16] X. Zhao, *J. Mater. Sci.* **2005**, *40*, 3423.

[17] X. Zhao, Y. Niu, X. Hu, *J. Polym. Sci., Part B: Polym. Phys.* **2005**, *43*, 1421.

[18] J. Wagner, Y. Song, T. Lee, H. E. Katz, *Electrochem. Sci. Adv.* **2022**, *2*, e2100165.

[19] H. Yano, K. Kudo, K. Marumo, H. Okuzaki, *Sci. Adv.* **2019**, *5*, eaav9492.

[20] A. Gadisa, W. D. Oosterbaan, K. Vandewal, J.-C. Bolsée, S. Bertho, J. D'Haen, L. Lutsen, D. Vanderzande, J. V. Manca, *Adv. Funct. Mater.* **2009**, *19*, 3300.

[21] Y. Liu, K. Xian, R. Gui, K. Zhou, J. Liu, M. Gao, W. Zhao, X. Jiao, Y. Deng, H. Yin, Y. Geng, L. Ye, *Macromolecules* **2022**, *55*, 133.

[22] S. Han, X. Jiang, Z. Yu, X. Wan, J. Zang, C. Zhang, H. Rui, X. Yang, A. Hagfeldt, L. Sun, *J. Mater. Chem. C* **2020**, *8*, 9236.

[23] P. Li, T. Lei, *J. Polym. Sci.* **2022**, *60*, 377.

[24] A. Giovannitti, D.-T. Sbircea, S. Inal, C. B. Nielsen, E. Bandiello, D. A. Hanifi, M. Sessolo, G. G. Malliaras, I. McCulloch, J. Rivnay, *Proc. Natl. Acad. Sci. U. S. A.* **2016**, *113*, 12017.

[25] C. B. Nielsen, A. Giovannitti, D.-T. Sbircea, E. Bandiello, M. R. Niazi, D. A. Hanifi, M. Sessolo, A. Amassian, G. G. Malliaras, J. Rivnay, I. McCulloch, *J. Am. Chem. Soc.* **2016**, *138*, 10252.

[26] M. Moser, L. R. Savagian, A. Savva, M. Matta, J. F. Ponder, T. C. Hidalgo, D. Ohayon, R. Hallani, M. Reisjalali, A. Troisi, A. Wadsworth, J. R. Reynolds, S. Inal, I. McCulloch, *Chem. Mater.* **2020**, *32*, 6618.

[27] L. Q. Flagg, C. G. Bischak, J. W. Onorato, R. B. Rashid, C. K. Luscombe, D. S. Ginger, *J. Am. Chem. Soc.* **2019**, *141*, 4345.

[28] A. A. Szumska, I. P. Maria, L. Q. Flagg, A. Savva, J. Surgailis, B. D. Paulsen, D. Moia, X. Chen, S. Griggs, J. T. Mefford, R. B. Rashid, A. Marks, S. Inal, D. S. Ginger, A. Giovannitti, J. Nelson, *J. Am. Chem. Soc.* **2021**, *143*, 14795.

[29] Y. Wang, E. Zeglio, H. Liao, J. Xu, F. Liu, Z. Li, I. P. Maria, D. Mawad, A. Herland, I. Mcculloch, W. Yue, *Chem. Mater.* **2019**, *31*, 9797.

[30] H. Ayalew, T. Wang, H. Yu, *Polymers* **2019**, *11*, 659.

[31] J. Hopkins, K. Fidanovski, L. Travaglini, D. Ta, J. Hook, P. Wagner, K. Wagner, A. Lauto, C. Cazorla, D. Officer, D. Mawad, *Chem. Mater.* **2022**, *34*, 140.

[32] C. Cendra, A. Giovannitti, A. Savva, V. Venkatraman, I. McCulloch, A. Salleo, S. Inal, J. Rivnay, *Adv. Funct. Mater.* **2019**, *29*, 1807034.

**ADVANCED
SCIENCE NEWS**

www.advancedsciencenews.com

**ADVANCED
MATERIALS
TECHNOLOGIES**

www.advmattechnol.de

[33] A. Savva, C. Cendra, A. Giugni, B. Torre, J. Surgailis, D. Ohayon, A. Giovannitti, I. McCulloch, E. Di Fabrizio, A. Salleo, J. Rivnay, S. Inal, *Chem. Mater.* **2019**, *31*, 927.

[34] S.-M. Kim, C.-H. Kim, Y. Kim, N. Kim, W.-J. Lee, E.-H. Lee, D. Kim, S. Park, K. Lee, J. Rivnay, M.-H. Yoon, *Nat. Commun.* **2018**, *9*, 3858.

[35] Z. Peng, L. Ye, H. Ade, *Mater. Horiz.* **2022**, *9*, 577.

[36] A. P. Hammersley, S. O. Svensson, M. Hanfland, A. N. Fitch, D. Häusermann, *J. Reticuloendothel. Soc.* **1996**, *14*, 235.

[37] X. Crispin, F. L. E. E. Jakobsson, A. Crispin, P. C. M. M. Grim, P. Andersson, A. Volodin, C. Van Haesendonck, M. Van Der Auweraer, W. R. Salaneck, M. Berggren, C. Van Haesendonck, M. Van Der Auweraer, W. R. Salaneck, M. Berggren, *Chem. Mater.* **2006**, *18*, 4354.

[38] A. R. Murphy, J. Liu, C. Luscombe, D. Kavulak, J. M. J. Fréchet, R. J. Kline, M. D. McGehee, *Chem. Mater.* **2005**, *17*, 4892.

[39] R. Mauer, M. Kastler, F. Laquai, *Adv. Funct. Mater.* **2010**, *20*, 2085.

[40] B. V. Khau, L. R. Savagian, M. De Keersmaecker, M. A. Gonzalez, E. Reichmanis, *ACS Mater. Lett.* **2019**, *1*, 599.

[41] M. Gu, L. Travaglini, J. Hopkins, D. Ta, A. Lauto, P. Wagner, K. Wagner, E. Zeglio, L. Jephcott, D. L. Officer, D. Mawad, *Synth. Met.* **2022**, *285*, 117029.

[42] E. G. Kim, J. L. Brédas, *J. Am. Chem. Soc.* **2008**, *130*, 16880.

[43] D. Bagayoko, *AIP Adv.* **2014**, *4*, 127104.

[44] J. Rivnay, P. Leleux, M. Ferro, M. Sessolo, A. Williamson, D. A. Koutsouras, D. Khodagholy, M. Ramuz, X. Strakosas, R. M. Owens, C. Benar, J.-M. Badier, C. Bernard, G. G. Malliaras, *Sci. Adv.* **2015**, *1*, e1400251.

[45] C. G. Bischak, L. Q. Flagg, D. S. Ginger, *Adv. Mater.* **2020**, *32*, 2002610.

[46] A. Savva, R. Hallani, C. Cendra, J. Surgailis, T. C. Hidalgo, S. Wustoni, R. Sheelamanthula, X. Chen, M. Kirkus, A. Giovannitti, A. Salleo, I. McCulloch, S. Inal, *Adv. Funct. Mater.* **2020**, *30*, 1907657.

[47] M. Moser, T. C. Hidalgo, J. Surgailis, J. Gladisch, S. Ghosh, R. Sheelamanthula, Q. Thiburce, A. Giovannitti, A. Salleo, N. Gasparini, A. Wadsworth, I. Zozoulenko, M. Berggren, E. Stavrinidou, S. Inal, I. McCulloch, *Adv. Mater.* **2020**, *32*, 2002748.

[48] D. Ohayon, A. Savva, W. Du, B. D. Paulsen, I. Uguz, R. S. Ashraf, J. Rivnay, I. McCulloch, S. Inal, *ACS Appl. Mater. Interfaces* **2021**, *13*, 4253.

[49] A. Giovannitti, I. P. Maria, D. Hanifi, M. J. Donahue, D. Bryant, K. J. Barth, B. E. Makdah, A. Savva, D. Moia, M. Zetek, P. R. F. Barnes, O. G. Reid, S. Inal, G. Rumbles, G. G. Malliaras, J. Nelson, J. Rivnay, I. McCulloch, *Chem. Mater.* **2018**, *30*, 2945.

[50] R. J. Kline, M. D. McGehee, *Polym. Rev.* **2006**, *46*, 27.

[51] A. P. Hammersley, *FIT2D: An Introduction and Overview*, **1997**, https://www.esrf.fr/computing/scientific/FIT2D/FIT2D_INTRO/fit2d.html (accessed: December 2022).

[52] V. V. Pavlishchuk, A. W. Addison, *Inorg. Chim. Acta* **2000**, *298*, 97.

[53] Katana, UNSW, Sydney, **2010**, https://doi.org/10.26190/669x-A286.

[54] G. Kresse, J. Furthmüller, *Phys. Rev. B* **1996**, *54*, 11169.

[55] J. P. Perdew, K. Burke, M. Ernzerhof, *Phys. Rev. Lett.* **1996**, *77*, 3865.

[56] S. Grimme, J. Antony, S. Ehrlich, H. Krieg, *J. Chem. Phys.* **2010**, *132*, 154104.

[57] L. Travaglini, A. P. Micolich, C. Cazorla, E. Zeglio, A. Lauto, D. Mawad, *Adv. Funct. Mater.* **2021**, *31*, 2007205.

[58] P. Schmode, D. Ohayon, P. M. Reichstein, A. Savva, S. Inal, M. Thelakkat, *Chem. Mater.* **2019**, *31*, 5286.

[59] D. A. Bernards, G. G. Malliaras, *Adv. Funct. Mater.* **2007**, *17*, 3538.